CHAPTER 9

Impact Dynamic Modeling and Adaptive Target Capture Control

The control of the tethered space system has received extensive attention with several articles published on the subject in recent years. Nakamura et al. [1] proposed a collaborative control method of the tension and thruster primarily during in the approach phase to the target. Modi et al. [2] designed an off-set control strategy that is implemented using a manipulator mounted on the platform to regulate the tether swing. A boundary control was proposed for station keeping of a tethered satellite system in the literature [3], but the proposed boundary controller does not constrain the tension in the tether to be positive. In Refs. [4–6], an arm link is used to control the attitude of the gripper attitude during the deployment phase, and a microgravity experiment was carried out to validate the feasibility of this scheme. Bergamaschi and Bonon [7] studied the coupling between the tether taut string vibrations and the satellite attitude motion. Wang et al. [8] proposed an attitude and orbit coordinated control method using mobile tether attachment point for tethered robot in approaching phase.

As one of the main research problems, target capture control [9,10] of a traditional space robot has been studied by many researchers. Wee and Walker [11] presented a general approach for modeling systems with a moving base and revealed that the impulse at contact could be minimized by the optimization of a scalar cost function. Hence, he proposed a joint space planning strategy that achieves both trajectory tracking and impact minimization. Aghili [12] proposed an optimal trajectory to intercept a grasping point on the target with zero relative velocity subject to the acceleration limit and adequate target alignment while minimizing the fly time and/or distance in the pregrasping phase. In the postgrasping phase, the manipulator damps out the targets' angular and linear momentums as quickly as possible; this is subject to the constraint that the magnitude of the exerted force and torque remain below their prespecified values. By using the bias momentum approach during the approaching phase, impedance control during the impact, and distributed momentum control during the postimpact phase,

Tethered Space Robot
https://doi.org/10.1016/B978-0-12-812309-6.00009-9

a possible control sequence for the successful completion of a capturing operation is proposed in Ref. [13]. Huang et al. [14] investigated a space robot system consisting of two arms, with one arm for accomplishing the capture mission, and the other one compensating for the disturbance of the base, and established a relationship between the motion of the two arms which can realize a zero reaction to the base. The literature [15] presents an autonomous motion control approach to generate the coordinated motion of a dual-arm space robot for target capturing. Luo and Sakawa [16] derived the equations of motion of the space robot by using the conservation law of linear and angular momenta, and then a sensory feedback control law that guarantees that both the position and orientation of the manipulator hand coincide asymptotically with those of the tumbling object. McCourt and De Silva [17] investigated the use of a model-based predictive control for the capture of a multidegrees-of-freedom object that moves in a somewhat predictable manner, using a deployable manipulator. Oki et al. [18] discussed a control strategy of a free- floating space robot for capturing a non-cooperative target, which includes both control methods simultaneously using the manipulator's redundancy. Moreover, a control law for reaction wheels is proposed so that the singularity problem would not happen.

Aghili [19] proposed a combined prediction and motion planning scheme, which was designed for a robotic capturing of a drifting and tumbling object with unknown dynamics using visual feedback. Besides, he [20] also suggested the guidance of a robot manipulator to capture a tumbling satellite with unknown dynamics parameters and then bring it to a state of rest. In the precapturing phase, the manipulator maneuvers are optimized by minimizing a cost function, which includes the time of travel and the weighted norms of the end-effector velocity and acceleration. For the problem of the capturing operation, a new optimal control method is designed by Huang et al. [21] to strengthen the control of the space robot with unknown factors. The robust control problem is translated into an optimal control problem, where the uncertainties are reflected in the objective function index, which is optimized. An optimal control strategy for a space robot to reach a tumbling object for capture with uncertainties in the initial and final boundary conditions was introduced in Ref. [22]. The objective of the strategy is to minimize the attitude disturbance applied to the base spacecraft due to the robot's approaching motion and the initial physical interception with the tumbling target object.

The literature mainly focuses on the strategy design for the precapture and postcapture control. Besides, the contact process of the capture operation is assumed to be completed in a short time and described by momentum

transfer. However, the dynamic collision process between the target and robot is quite complicated during the capture operation. Therefore it is quite significant to guarantee the stabilization of the robot during target capture. In Ref. [23], a force tracking strategy inspired by a human control system is added to the multiple impedance control (MIC) algorithm and the general formulation is revised to fulfill a desired force tracking strategy for object manipulation tasks. The stability analysis of the MIC algorithm based on the Liapunov Direct Method, besides error analysis, shows that good tracking of cooperative manipulators and the manipulated object is guaranteed. Besides, he [24] also proposed a MIC law to manipulate space objects by multiple arms of space free-flying robots (SFFR), which is based on the concept of designated impedances and enforces them at various system levels. Nakanishi and Yoshida [25] proposed a impedance control for a space manipulator in the contact phase of target capture. Abiko et al. [26] addressed an impedance control for a free-floating space robot in the grasping of a tumbling target with model uncertainty. The concept of a "Dynamic grasping area" is introduced by Cheng et al. [27] to describe the dynamic collision process of target capture and designed an ideal grasping strategy based on the finding that if the product of the speed control parameter and dB adjustment parameter is close to, but smaller than, the minimum grasping speed, collision impact in the grasping process could be reduced greatly.

The literature related to the TSR mentioned in this chapter thus far all focus on the control during deployment or station-keeping phase, and few researches on target capture control of the TSR exists so far. Besides, due to the presence of the space tether, the capture dynamic characteristics of the TSR are different with the aforementioned characteristics of a traditional space robot. The dynamic coupling between the TSR and the space tether is quite complicated and it is a challenge to design the stabilization controller for the TSR during target capture. Therefore the objective of this chapter is to investigate the control problem of the TSR during the capture phase and propose an adaptive robust control law with the consideration of the uncertainties in the dynamic model.

9.1 DYNAMIC MODELING OF TETHERED SPACE ROBOTS FOR TARGET CAPTURE

As shown in Fig. 9.1, the gripper of the TSR is released from the space platform and captures a target. The related frames are: $Oxyz$ is the platform orbital frame with its origin located at the centroid of the space platform. The axes of the coordinate are oriented as follows: the x-axis is collinear with a line that extends from the center of the Earth to the centroid of the space

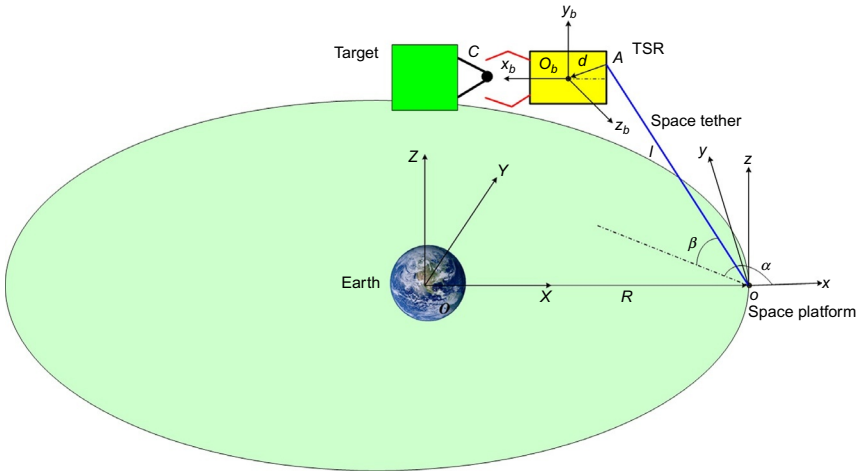

Fig. 9.1 Target capture by the TSR.

platform, the y-axis is in the orbital plane in the local horizontal direction, and the z-axis is along the orbital normal and completes a right-handed triad. $O_b x_b y_b z_b$ is the TSR body frame with its origin O_b located at the centroid of the gripper of the TSR. A is the tether attachment point and $\boldsymbol{d}$ represents the corresponding position vector from A to O_b. C is the component of target captured by the TSR.

9.1.1 Dynamic Modeling of the TSR

The following assumptions are made:

(1) The platform is point mass with its motion prescribed on a circular orbit. Furthermore, the mass of the platform is assumed to be much bigger than that of the gripper. Therefore the influence of the gripper on the motion of the platform is ignored.

(2) The elasticity of space tether is ignored and the space tether is uniform in mass.

(3) For simplicity, the gripper is considered as one rigid body.

The orbital radius of the platform is R_0 and the position vector from the earth to the platform in $Oxyz$ is given as:

$$\boldsymbol{R}_0 = R_0 \boldsymbol{i} \tag{9.1}$$

where $\boldsymbol{i}$, $\boldsymbol{j}$, and $\boldsymbol{k}$ are the unit vectors of the platform orbital frame.

The velocity of the platform is given as:

$$\boldsymbol{V}_0 = \boldsymbol{\omega} \times \boldsymbol{R}_0 \tag{9.2}$$

l, α, and β denote length, in-plane angle, and out-of-plane angle of the space tether as shown in Fig. 9.1. Then the space tether vector $\boldsymbol{l}$, that is the position vector of the tether attachment point A, is expressed as:

$$\boldsymbol{l} = l\cos\alpha\cos\beta\boldsymbol{i} + l\sin\alpha\cos\beta\boldsymbol{j} + l\sin\beta\boldsymbol{k} \tag{9.3}$$

The relative attitude angles from the platform orbital frame $Oxyz$ to TSR body frame $O_bx_by_bz_b$ are defined by the Euler angle, the roll angle φ, the pitch angle θ, and the yaw angle ψ of the 1-2-3 Euler rotation sequence. The transformation matrix $\boldsymbol{R}(\varphi,\theta,\psi)$ from the platform orbital frame $Oxyz$ to the TSR body frame $O_bx_by_bz_b$ is expressed as follows:

$$\begin{aligned}&\boldsymbol{R}(\varphi,\theta,\psi)\\ &= \begin{bmatrix} \cos\psi cos\theta & \cos\psi sin\varphi sin\theta - sin\psi cos\varphi & \cos\psi\cos\varphi sin\theta + sin\varphi sin\psi \\ \sin\psi\cos\theta & \sin\psi\sin\varphi\sin\theta + \cos\psi\cos\varphi & \sin\psi\cos\varphi\sin\theta - \cos\psi\sin\varphi \\ -\sin\theta & \sin\varphi\cos\theta & \cos\varphi\cos\theta \end{bmatrix}\end{aligned}$$

The angular velocity of the TSR in $O_bx_by_bz_b$ can be obtained:

$$\boldsymbol{\omega}_b = \left(\dot{\theta}\sin\psi + \dot{\varphi}cos\theta cos\psi\ \dot{\theta}\cos\psi - \dot{\varphi}\cos\theta\sin\psi\ \dot{\varphi}\sin\theta + \dot{\psi}\right)^T \tag{9.4}$$

Therefore $\boldsymbol{d}$ is given by:

$$\boldsymbol{d} = \boldsymbol{R}_{ob}{}^{-1}\boldsymbol{d}_b \tag{9.5}$$

with $\boldsymbol{d}_b = \left(d_x\ d_y\ d_z\right)^T$ the position vector from A to O_b expressed in $O_bx_by_bz_b$.

The position of the TSR is:

$$\boldsymbol{R}_b = \boldsymbol{R}_0 + \boldsymbol{r}_b \tag{9.6}$$

where

$$\boldsymbol{r}_b = \boldsymbol{l} + \boldsymbol{d}$$

The velocity of the TSR is:

$$\boldsymbol{V}_b = \boldsymbol{V}_0 + \dot{\boldsymbol{r}}_b + \boldsymbol{\omega}\times\boldsymbol{r}_b \tag{9.7}$$

(1) Kinetic energy of the system

The kinetic energy of the platform is given as:

$$\boldsymbol{T}_p = \frac{1}{2}\boldsymbol{V}_0^T(M - m_l)\boldsymbol{V}_0 \tag{9.8}$$

where M denotes the mass of the space platform and the space tether; ρ is the density of the space tether. Therefore $m_l = \rho l$ denotes the mass of the released space tether.

The velocity of an arbitrary point on the space tether is given as:

$$\boldsymbol{V}_L = \boldsymbol{V}_0 + \dot{\boldsymbol{r}}_L + \boldsymbol{\omega} \times \boldsymbol{r}_L \tag{9.9}$$

Then, the kinetic energy of the space tether is obtained:

$$\boldsymbol{T}_l = \int_0^l \frac{1}{2} \boldsymbol{V}_L^T \boldsymbol{V}_L \rho dL \tag{9.10}$$

The linear kinetic energy of the TSR is:

$$\boldsymbol{T}_r = \frac{1}{2} \boldsymbol{V}_b^T m \boldsymbol{V}_b \tag{9.11}$$

The angular kinetic energy of the space tether:

$$\boldsymbol{T}_a = \frac{1}{2} \boldsymbol{\omega}_b^T \boldsymbol{I} \boldsymbol{\omega}_b \tag{9.12}$$

Therefore the kinetic energy of the whole system is:

$$\boldsymbol{T} = \boldsymbol{T}_r + \boldsymbol{T}_a + \boldsymbol{T}_p + \boldsymbol{T}_l \tag{9.13}$$

(2) Potential energy of the system

The potential energy of the platform is given as:

$$\boldsymbol{V}_p = -\mu_e \frac{M - m_l}{|\boldsymbol{R}_0|} \tag{9.14}$$

The potential energy of the gripper is:

$$\boldsymbol{V}_r = -\mu_e \frac{\boldsymbol{m}}{|\boldsymbol{r_b} + \boldsymbol{R}_0|} \tag{9.15}$$

where μ_e denotes the gravitational constant of the Earth.

The position of an arbitrary point along the space tether is given as:

$$\boldsymbol{L} = L \cos\alpha \cos\beta \boldsymbol{i} + L \sin\alpha \cos\beta \boldsymbol{j} + L \sin\beta \boldsymbol{k}$$

The potential energy of the space tether is given as:

$$\boldsymbol{V}_l = \int_0^l \frac{-\mu_e \rho}{|\boldsymbol{L} + \boldsymbol{R}_0|} dL \tag{9.16}$$

Using Taylor's expansion formula, Eqs. (9.14)–(9.16) can be simplified. Therefore the potential energy of the whole system is:

$$\boldsymbol{V} = \boldsymbol{V}_p + \boldsymbol{V}_l + \boldsymbol{V}_r \tag{9.17}$$

Applying Lagrange's equations, the equations of motions of the TSR can be obtained

$$\frac{\mathrm{d}}{\mathrm{d}t}\left(\frac{\partial T}{\partial \dot{\boldsymbol{q}}}\right)-\frac{\partial T}{\partial \boldsymbol{q}}+\frac{\partial V}{\partial \boldsymbol{q}}=Q_q \tag{9.18}$$

where

$$\boldsymbol{q}=l,\ \alpha,\ \beta,\ \varphi,\ \theta,\ \psi$$

For convenience, neglect the out-of-plane motion of the space tether and simplify Eq. (9.18), we have:

$$\boldsymbol{M}(\boldsymbol{\xi})\ddot{\boldsymbol{\xi}}+\boldsymbol{N}\left(\boldsymbol{\xi},\dot{\boldsymbol{\xi}}\right)\dot{\boldsymbol{\xi}}+\boldsymbol{G}(\boldsymbol{\xi})=\boldsymbol{Q} \tag{9.19}$$

where

$$\xi=[l\,\alpha\,\psi]^{\mathrm{T}};\quad \boldsymbol{Q}=\left[Q_l\ \frac{Q_\alpha}{l}\ Q_\psi\right]^{\mathrm{T}};$$

$$\boldsymbol{M}(\boldsymbol{\xi})=\begin{bmatrix} m & 0 & md_{1x} \\ 0 & ml & -md_{2\gamma} \\ md_{1x} & -mld_{2\gamma} & \left(\boldsymbol{I}_z+md_x^2+md_\gamma^2\right)\end{bmatrix};$$

$$\boldsymbol{N}\left(\boldsymbol{\xi},\dot{\boldsymbol{\xi}}\right)=\begin{bmatrix} 0 & -ml(\dot{\alpha}+2\omega) & md_2(-\dot{\psi}+2\omega) \\ m(\dot{\alpha}+2\omega) & m\dot{l} & -md_1(\dot{\psi}+2\omega) \\ m(-\dot{\alpha}-2\omega)d_2 & md_1\left(\dot{l}-l\dot{\alpha}-2l\omega\dot{\alpha}\right) & 0\end{bmatrix};$$

$$\boldsymbol{G}(\boldsymbol{\xi})\quad =\begin{bmatrix} -3m\omega^2\cos\alpha(d_2+l\cos\alpha) \\ 3m\omega^2\sin\alpha(d_2+l\cos\alpha) \\ -3m\omega^2d_1d_2-3m\omega^2d_1l\cos\alpha\end{bmatrix};$$

$$\begin{cases} d_{1x}=-d_x\sin(\psi+\alpha)+d_y\cos(\psi+\alpha) \\ d_{2\gamma}=d_x\cos(\psi+\alpha)+d_y\sin(\psi+\alpha)\end{cases};\quad \begin{cases} d_1=-d_x\sin\psi+d_y\cos\psi \\ d_2=d_x\cos\psi+d_y\sin\psi\end{cases}$$

Similar to the dynamic equations of the space robot [28], the following properties are satisfied for Eq. (9.19):

(1) $\boldsymbol{M}(\boldsymbol{\xi})$ is a symmetric positive definite matrix and uniformly bounded and satisfies the following equation:

$$\gamma_1\boldsymbol{I}_3\le\boldsymbol{M}(\boldsymbol{\xi})\le\gamma_2\boldsymbol{I}_3$$

where γ_1 and γ_2 are two positive constants.

(2) $\dot{\boldsymbol{M}}(\boldsymbol{\xi}) - 2\boldsymbol{N}\left(\boldsymbol{\xi}, \dot{\boldsymbol{\xi}}\right)$ is skew-symmetric and $\boldsymbol{\xi}^T\left(\dot{\boldsymbol{M}}(\boldsymbol{\xi}) - 2\boldsymbol{N}\left(\boldsymbol{\xi}, \dot{\boldsymbol{\xi}}\right)\right)\boldsymbol{\xi} = 0$ holds for $\forall \boldsymbol{\xi} \in R^3$.

(3) $\boldsymbol{M}(\boldsymbol{\xi})\ddot{\boldsymbol{\xi}} + \boldsymbol{N}\left(\boldsymbol{\xi}, \dot{\boldsymbol{\xi}}\right)\dot{\boldsymbol{\xi}} + \boldsymbol{G}(\boldsymbol{\xi})$ cannot be linearized. However, assume $\boldsymbol{\delta} = \left[0, 0, -3m\omega^2 d_1 d_2\right]^T$ and $\boldsymbol{M}(\boldsymbol{\xi})\ddot{\boldsymbol{\xi}} + \boldsymbol{N}\left(\boldsymbol{\xi}, \dot{\boldsymbol{\xi}}\right)\dot{\boldsymbol{\xi}} + \boldsymbol{G}(\boldsymbol{\xi}) - \boldsymbol{\delta}$ can be linearized. Besides, the orbital angular velocity ω is small and $\boldsymbol{\delta}$ can be treated as a disturbance.

9.1.2 Dynamic Modeling of the Target

Compared with the orbit period, the time for a capture mission is usually very small. Therefore we ignore the effect of orbit on the target motion, and establish a simply target dynamic model as follows:

$$m_t \ddot{\boldsymbol{X}} = \boldsymbol{f}_t \tag{9.20}$$

where m_t is the mass of the target; $\boldsymbol{X} = \left[x_t\, y_t\, z_t\right]^T \in R^3$ denotes the target position in the platform orbital frame, and $\boldsymbol{f}_t = \left[f_{tx} f_{ty} f_{tz}\right]^T \in R^3$ the corresponding impact force during the target capture phase.

Assume the target is a rigid body and its attitude dynamic equation can be given by the following equation:

$$\boldsymbol{I}_t \dot{\boldsymbol{\omega}}_t = -\boldsymbol{\omega}_t^{\times} \boldsymbol{I}_t \boldsymbol{\omega}_t + \boldsymbol{T}_t \tag{9.21}$$

where $\boldsymbol{\omega}_t = \left[\omega_{tx}\, \omega_{ty}\, \omega_{tz}\right]^T \in R^3$ denotes the absolute angular velocity of the target expressed in the target body frame; $\boldsymbol{I}_t \in R^{3\times 3}$ is the inertia matrix of the target. $\boldsymbol{T}_t \in R^3$ denotes the torque caused by the impact force. $\boldsymbol{\omega}_t^{\times}$ is the skew-symmetric matrix of $\boldsymbol{\omega}_t$.

The MPR [24] are used to describe the kinematics model of the target attitude as follows:

$$\dot{\boldsymbol{\sigma}}_t = G(\boldsymbol{\sigma}_t)\boldsymbol{\omega}_t \tag{9.22}$$

where $\boldsymbol{\sigma} = \left[\sigma_1\, \sigma_2\, \sigma_3\right]^T \in R^3$ and $G(\boldsymbol{\sigma})$ is defined as follows:

$$G(\boldsymbol{\sigma}_t) = \frac{1}{4}\left[\left(1 - \boldsymbol{\sigma}_t^T \boldsymbol{\sigma}_t\right) I + 2\boldsymbol{\sigma}_t^{\times} + 2\boldsymbol{\sigma}_t \boldsymbol{\sigma}_t^T\right]$$

where $\mathbf{I}$ is a 3×3 unit matrix.

9.1.3 Impact Dynamic Models for the TSR Capturing a Target

As shown in Fig. 9.2, the gripper of the TSR is mainly composed of three fingers, including $a_0a_1a_2$, $b_0b_1b_2$, and $c_0c_1c_2$. a_0, a_1, b_0, b_1, c_0, and c_1 are six joints, around which each correspond link can rotate in the x-y plane of

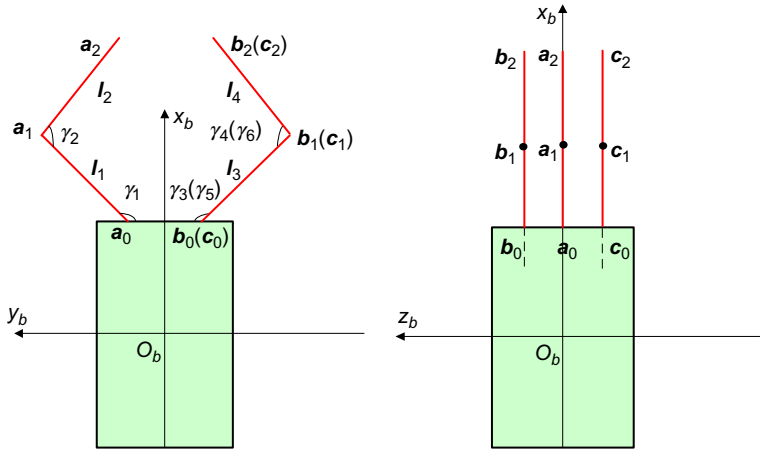

Fig. 9.2 Structure of the TSR's gripper.

the TSR body frame. γ_i $(i=1,\ldots,6)$ is the joint angle. Moreover, each link is assumed to be a cylinder with a radius of r_g.

Assume there exists a stick-like component t_1t_2 on the target as represented in Fig. 9.3, which is designed to be captured by the gripper of the TSR in the mission. The component t_1t_2 is also assumed to be a cylinder handle with a radius of r_t.

In the target capture process, the TSR's gripper constricts and collides with the handle of target, and the impact forces occur along the direction of the common normal line at the contact point. Define the contact deformation, which is the intrusion value inside of both the gripper and target, as δ. When $\delta<0$, collision occurs.

Hertz model is introduced to describe the impact forces of gripper:

$$\boldsymbol{F}_{\mathrm{rt}}=k_{\mathrm{g}}|\delta|\boldsymbol{n}+k_{\mathrm{c}}\dot{\delta}\boldsymbol{n} \tag{9.23}$$

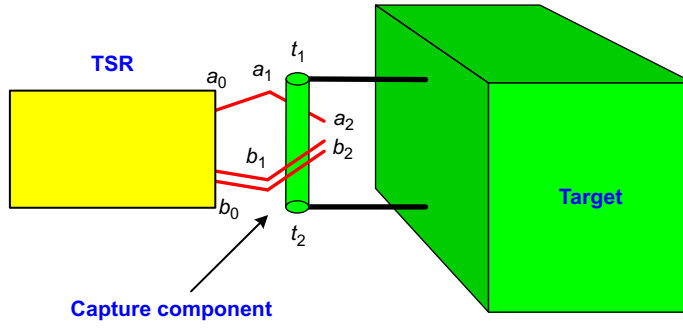

Fig. 9.3 Capture component of target.

where k_g and k_c are stiffness and damping coefficients of contact impact, $\boldsymbol{n}$ is the unit vector of common normal line at the contact point.

The relationship between the external forces $\boldsymbol{F}_{rt}$ on the TSR's gripper and impact forces $\boldsymbol{F}_{tr}$ on target is as follows:

$$\boldsymbol{F}_{rt} = -\boldsymbol{F}_{tr} \tag{9.24}$$

Define the relative position between the contact point and the centroid of the TSR as $\boldsymbol{d}_r$, and the torque on the TSR caused by the impact force can be obtained:

$$\boldsymbol{T}_{rt} = \boldsymbol{d}_r \times \boldsymbol{F}_{rt} \tag{9.25}$$

Similarly, the torque on the target caused by the impact force is:

$$\boldsymbol{T}_{tr} = \boldsymbol{d}_t \times \boldsymbol{F}_{tr} \tag{9.26}$$

where $\boldsymbol{d}_t$ denotes the relative position between the contact point and the centroid of target.

9.2 STABILIZATION CONTROLLER DESIGN FOR TARGET CAPTURE BY TSR

In this section, the target capture controller of the TSR is designed. At first, impedance control of the TSR is utilized and derived for the target capture operation. Then, in order to guarantee a steady and successful target operation, an adaptive controller is proposed to adjust the pose of the TSR during target capture.

9.2.1 Impedance Control

Position-based impedance control (PBIC) is an effective method to deal with the dynamic relationship between the contact force and relative position of the gripper and target [29]. In a PBIC-based control scheme, the outer control loop converts the sensed forces into modifications for the reference signals, which is used as input of the inner position controller. Therefore PBIC is used in the controller design of the target capture for the gripper of the TSR.

Applying the traditional PBIC for the gripper yields:

$$\boldsymbol{M}\ddot{\boldsymbol{E}} + \boldsymbol{B}\dot{\boldsymbol{E}} + \boldsymbol{K}\boldsymbol{E} = -\boldsymbol{F}_e \tag{9.27}$$

where $\boldsymbol{M}$ denotes the positive definite diagonal inertia matrix, $\boldsymbol{B}$ the positive definite diagonal damping matrix, and $\boldsymbol{K}$ the positive definite diagonal stiffness matrix; $\boldsymbol{E} = \boldsymbol{x}_d - \boldsymbol{x}_r$, where $\boldsymbol{E}$ denotes the modification value of the

reference trajectory $\boldsymbol{x}_r$ designed for the TSR, $\boldsymbol{x}_d$ is the regulated trajectory; $\boldsymbol{F}_e$ is the impact forces between the gripper of the TSR and the target, which is obtained by the force sensor mounted on the gripper.

Given the characteristics of the gripper of the TSR used in Fig. 9.4, we find that the target may collide with the gripper on at most seven places at one time. Therefore rewrite Eq. (9.27) as follows:

$$\boldsymbol{M}_d\ddot{\boldsymbol{e}}_i + \boldsymbol{B}_d\dot{\boldsymbol{e}}_i + \boldsymbol{K}_d\boldsymbol{e}_i = -\boldsymbol{F}_{ei} \tag{9.28}$$

where $\boldsymbol{e}_i$ $(i = 1, 2, \ldots, 7)$ is the ith modification value of the reference trajectory due to the impact force $\boldsymbol{F}_{ei}$.

Impedance function in Eq. (9.28) can be expressed in the frequency domain:

$$\boldsymbol{e}_i(\boldsymbol{s}) = \frac{-\boldsymbol{F}_{ei}}{\boldsymbol{M}_d\boldsymbol{s}^2 + \boldsymbol{B}_d\boldsymbol{s} + \boldsymbol{K}_d} \tag{9.29}$$

Applying the regulation value $\boldsymbol{e}_i$ to adjusting the reference trajectory $\boldsymbol{x}_r$ yields the regulated trajectory $\boldsymbol{x}_d$ as follows:

$$\boldsymbol{x}_d = \boldsymbol{x}_r + \sum_{i=1}^{7} \boldsymbol{e}_i \tag{9.30}$$

Obviously, when collisions between the gripper and target do not occur, $\boldsymbol{F}_e = \boldsymbol{0}$ and $\boldsymbol{e}_i = \boldsymbol{0}$. At this time $\boldsymbol{x}_d = \boldsymbol{x}_r$ and the TSR will track the designed reference trajectory $\boldsymbol{x}_r$ without any regulation to capture target.

The PBIC-based control scheme is detailed in Fig. 9.5.

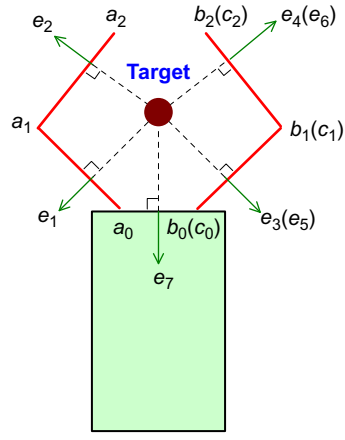

Fig. 9.4 Collisions of the TSR during target capture.

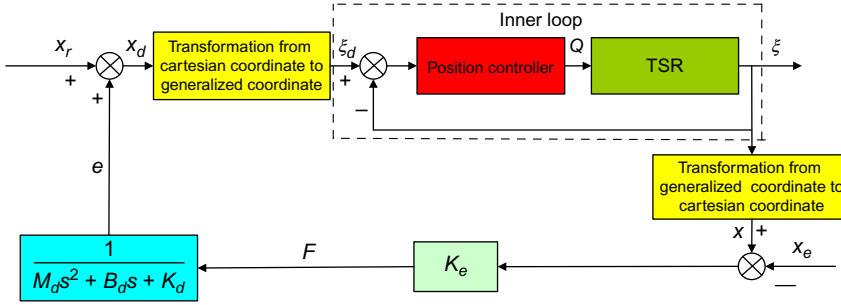

Fig. 9.5 PBIC-based control scheme of TSR for target capture.

9.2.2 Adaptive Robust Target Capture Control

In the previous section, the PBIC-based control scheme is proposed to regulate the trajectory of the TSR during target capture. In this section, an adaptive and robust inner position controller is proposed to realize the tracking control of the TSR.

The system parameters of the TSR, including the mass, inertial matrix, and centroid position, change during target capture, and the uncertainties of these parameters mainly come from (1) the fuel consumption during target capture (2) the motions of the gripper (although the influence of the gripper is not considered in the dynamic modeling for simplicity, we can convert this influence to the uncertainty of the whole gripper parameters). These uncertainties may exert an influence on the target capture operation of the TSR. Therefore we will design adaptive target capture control methods to overcome this influence and enhance the control performance of the TSR during target capture.

The dynamic model of the TSR in Eq. (9.19) can be rewritten as:

$$(\boldsymbol{M}_0 + \Delta\boldsymbol{M})\ddot{\boldsymbol{\xi}} + (\boldsymbol{N}_0 + \Delta\boldsymbol{N})\dot{\boldsymbol{\xi}} + (\boldsymbol{G}_0 + \Delta\boldsymbol{G}) = \boldsymbol{Q} \tag{9.31}$$

where $\boldsymbol{M}_0$, $\boldsymbol{N}_0$, and $\boldsymbol{G}_0$ are the nominal matrices of $\boldsymbol{M}$, $\boldsymbol{N}$, and $\boldsymbol{G}$; $\Delta\boldsymbol{M}$, $\Delta\boldsymbol{N}$, and $\Delta\boldsymbol{G}$ are the uncertainties due to the fuel consumption and motions of the gripper although the motions of the gripper are not considered in the dynamic modeling. They satisfy the following relationship:

$$\begin{cases} \boldsymbol{M} = \boldsymbol{M}_0 + \Delta\boldsymbol{M} \\ \boldsymbol{N} = \boldsymbol{N}_0 + \Delta\boldsymbol{N} \\ \boldsymbol{G} = \boldsymbol{G}_0 + \Delta\boldsymbol{G} \end{cases} \tag{9.32}$$

Define the tracking errors as:

$$\boldsymbol{e} = \boldsymbol{\xi}_d - \boldsymbol{\xi} \tag{9.33}$$

where $\boldsymbol{\xi}_d$ is the desired system state.

Define the error function as:

$$\boldsymbol{r} = \dot{\boldsymbol{e}} + \boldsymbol{\Lambda e} = \dot{\boldsymbol{\xi}}_d - \dot{\boldsymbol{\xi}} + \boldsymbol{\Lambda e} \tag{9.34}$$

where $\boldsymbol{\Lambda}$ is a symmetrical positive-definite matrix.

Then the error dynamic model is given as:

$$\begin{aligned} \boldsymbol{M}_0\dot{\boldsymbol{r}} &= \boldsymbol{M}_0(\ddot{\boldsymbol{e}} + \boldsymbol{\Lambda}\dot{\boldsymbol{e}}) \\ &= \boldsymbol{M}_0\left(\ddot{\boldsymbol{\xi}}_d + \boldsymbol{\Lambda}\dot{\boldsymbol{e}}\right) + \boldsymbol{N}_0\left(\dot{\boldsymbol{\xi}}_d + \boldsymbol{\Lambda e}\right) - \boldsymbol{N}_0\left(\dot{\boldsymbol{\xi}}_d + \boldsymbol{\Lambda e} - \dot{\boldsymbol{\xi}}\right) \\ &\quad + \boldsymbol{G}_0 + \Delta\boldsymbol{M}\ddot{\boldsymbol{\xi}} + \Delta\boldsymbol{N}\dot{\boldsymbol{\xi}} + \Delta\boldsymbol{G} - \boldsymbol{Q} \\ &= \boldsymbol{M}_0\left(\ddot{\boldsymbol{\xi}}_d + \boldsymbol{\Lambda}\dot{\boldsymbol{e}}\right) + \boldsymbol{N}_0\left(\dot{\boldsymbol{\xi}}_d + \boldsymbol{\Lambda e}\right) - \boldsymbol{N}_0\boldsymbol{r} + \boldsymbol{G}_0 + \boldsymbol{\rho} - \boldsymbol{Q} \end{aligned} \tag{9.35}$$

where $\boldsymbol{\rho} = \Delta\boldsymbol{M}\ddot{\boldsymbol{\xi}} + \Delta\boldsymbol{N}\dot{\boldsymbol{\xi}} + \Delta\boldsymbol{G}$ is the uncertainty.

Rewrite Eq. (9.35) as:

$$\boldsymbol{M}_0\dot{\boldsymbol{r}} + \boldsymbol{N}_0\boldsymbol{r} = \boldsymbol{M}_0\left(\ddot{\boldsymbol{\xi}}_d + \boldsymbol{\Lambda}\dot{\boldsymbol{e}}\right) + \boldsymbol{N}_0\left(\dot{\boldsymbol{\xi}}_d + \boldsymbol{\Lambda e}\right) + \boldsymbol{G}_0 + \boldsymbol{\rho} - \boldsymbol{Q} \tag{9.36}$$

where $\boldsymbol{\rho} = \Delta\boldsymbol{M}\ddot{\boldsymbol{\xi}} + \Delta\boldsymbol{N}\dot{\boldsymbol{\xi}} + \Delta\boldsymbol{G}$ is the uncertainty in the dynamic model of the TSR.

In this work, the NN is used to estimate the uncertainty of the system. Therefore a robust and adaptive control law based on the NN is given as:

$$\boldsymbol{Q} = \boldsymbol{K}\boldsymbol{r} + \boldsymbol{M}_0\left(\ddot{\boldsymbol{\xi}}_d + \boldsymbol{\Lambda}\dot{\boldsymbol{e}}\right) + \boldsymbol{N}_0\left(\dot{\boldsymbol{\xi}}_d + \boldsymbol{\Lambda e}\right) + \boldsymbol{G}_0 + \hat{\boldsymbol{\rho}} + \boldsymbol{\eta} \tag{9.37}$$

where $\hat{\boldsymbol{\rho}}$ is the estimated uncertainty of the TSR via the NN and $\boldsymbol{\eta}$ a robust term.

Substitute control law Eq. (9.37) into (9.36), we have:

$$\boldsymbol{M}_0\dot{\boldsymbol{r}} = -\boldsymbol{N}_0\boldsymbol{r} - \boldsymbol{K}\boldsymbol{r} + \widetilde{\boldsymbol{\rho}} + \boldsymbol{\delta} - \boldsymbol{\eta} \tag{9.38}$$

where $\boldsymbol{\delta}$ is the estimation error of the NN.

It can be seen that $\boldsymbol{\rho} = \boldsymbol{\rho}\left(\dot{\boldsymbol{\xi}}, \boldsymbol{\xi}\right)$ is the function of $\dot{\boldsymbol{\xi}}$ and $\boldsymbol{\xi}$. Therefore the inputs of the RBF NN are $\dot{\boldsymbol{\xi}}$ and $\boldsymbol{\xi}$. The estimated value $\hat{\boldsymbol{\rho}}$ can be expressed as:

$$\hat{\boldsymbol{\rho}} = \hat{\boldsymbol{\Theta}}^T\boldsymbol{\Phi}_\rho \tag{9.39}$$

where $\hat{\boldsymbol{\Theta}}$ is the weight matrix and $\boldsymbol{\Phi}_\rho$ the RBF function, which is defined as:

$$\boldsymbol{\Phi}_{\rho i}(\boldsymbol{Y}) = \exp\left(-\frac{\|\boldsymbol{Y} - C_i\|^2}{2\sigma_i^2}\right) \tag{9.40}$$

where $\boldsymbol{Y}$ is the input of the RBF NN function, C_i denotes the center values of the ith neuron and σ_i the width of the ith neuron.

The adaptive law [30] for $\hat{\Theta}$ is designed as:

$$\dot{\hat{\Theta}} = \boldsymbol{F}_\rho \boldsymbol{\Phi}_\rho \boldsymbol{r}^T - k_\rho \boldsymbol{F}_\rho \|\boldsymbol{r}\| \hat{\Theta} \tag{9.41}$$

where $\boldsymbol{F}_\rho$ is a positive-definite matrix and k_ρ is a positive design parameter.

When the RBF-based NN is used to estimate the uncertainty, there exists estimation error $\widetilde{\boldsymbol{\rho}}$, which is compensated by the robust term $\boldsymbol{\eta}$:

$$\boldsymbol{\eta} = \eta_{\boldsymbol{\delta}} \cdot \operatorname{sgn}(\boldsymbol{r}) \tag{9.42}$$

where $\operatorname{sgn}(\cdot)$ is a sign function and $\eta_{\tilde{\rho}}$ is the upper bound of estimation error $\widetilde{\boldsymbol{\rho}}$.

Chattering may occur in the control system for the sign function in Eq. (9.42). To solve this problem, the sign function can be modified into the saturation functions:

$$sat(\boldsymbol{r}_i, \varepsilon) = \begin{cases} 1 & \boldsymbol{r}_i > \varepsilon \\ \boldsymbol{r}_i/\varepsilon & -\varepsilon \le \boldsymbol{r} \le \varepsilon_i \\ -1 & \boldsymbol{r}_i < -\varepsilon \end{cases}$$

where $i = 1,2,3$ and ε is a positive number.

The desired operation trajectory is obtained in the following ways: assume the aim of the TSR target capture control as adjusting the pose of the TSR so that the capture component of target goes into the capture area of the gripper and keeps coinciding with the center of the capture area during the folding of the gripper.

Define the desired position of gripper as $\boldsymbol{x}_d$. It can be seen that $\boldsymbol{x}_d$ is decided by three variables, including l, α, and ψ. Given the influences of the l, α, and ψ, we choose to determine ψ at first with the consideration of target capture mission requirements. Then $\boldsymbol{x}_d$ corresponds to a unique solution of l, α for a given ψ.

Given the characteristics of the capture component of the target proposed in this study, we choose $\psi_r = \psi_t$ as the desired capture attitude for simplicity. Of course, there exist many other attitudes that are suitable for a target capture mission.

Define the position of the center of the capture area with respect to the centroid of the gripper as $\boldsymbol{h}$ in the TSR body frame $O_b x_b y_b z_b$, and assume the vector from the tether attachment point to the centroid of the gripper as $\boldsymbol{d}_b$ in $O_b x_b y_b z_b$. Therefore the desired position of the center of the capture area $\boldsymbol{x}_d$,

the desired tether length l_r, and the desired in-plane angle α_r satisfy the following relationship:

$$\boldsymbol{x}_d = \boldsymbol{R}(\psi_r)(\boldsymbol{d}_b + \boldsymbol{h}) + \boldsymbol{l}_r(l_r, \alpha_r) \tag{9.43}$$

where the transformation matrix $\boldsymbol{R}(\psi_r) = \begin{bmatrix} \cos\psi_r & -\sin\psi_r & 0 \\ \sin\psi_r & \cos\psi_r & 0 \\ 0 & 0 & 1 \end{bmatrix}$ and $\boldsymbol{l}_r$ is the desired vector of space tether.

From Eq. (9.43), $\boldsymbol{l}_r$ can be obtained:

$$\boldsymbol{l}_r(l_r, \alpha_r) = \boldsymbol{x}_d - \boldsymbol{R}(\psi_r)(\boldsymbol{d}_b + \boldsymbol{h}) \tag{9.44}$$

Besides, $\boldsymbol{l}_r$ can be expressed as follows:

$$\boldsymbol{l}_r = l_r \begin{bmatrix} \cos\alpha_r \\ \sin\alpha_r \end{bmatrix} \tag{9.45}$$

By combining Eqs. (9.44) and (9.45), l_r and α_r can be obtained:

$$\begin{cases} l_r = \|\boldsymbol{l}_r\| \\ \alpha_r = \arcsin\left(\dfrac{\boldsymbol{l}_{r2}}{l}\right) \end{cases} \tag{9.46}$$

where $\boldsymbol{l}_{r2}$ is the second element of $\boldsymbol{l}_r$.

Choose the Lyapunov function as:

$$V = \frac{1}{2}\boldsymbol{r}^T\boldsymbol{M}_0\boldsymbol{r} + \frac{1}{2}tr\left(\widetilde{\boldsymbol{\Theta}}^T\boldsymbol{F}_\rho^{-1}\widetilde{\boldsymbol{\Theta}}\right) \tag{9.47}$$

where M_0 is a positive-define matrix; F_ρ is a positive-define design matrix; Therefore $V \geq 0$ holds.

Taking the derivative of V yields:

$$\dot{V} = \boldsymbol{r}^T\boldsymbol{M}_0\dot{\boldsymbol{r}} + \frac{1}{2}\boldsymbol{r}^T\dot{\boldsymbol{M}}_0\boldsymbol{r} + tr\left(\widetilde{\boldsymbol{\Theta}}^T\boldsymbol{F}_\rho^{-1}\dot{\widetilde{\boldsymbol{\Theta}}}.\right) \tag{9.48}$$

Substituting Eq. (9.38) into (9.48), we have:

$$\begin{aligned} \dot{V} &= \boldsymbol{r}^T\boldsymbol{M}_0\dot{\boldsymbol{r}} + \frac{1}{2}\boldsymbol{r}^T\dot{\boldsymbol{M}}_0\boldsymbol{r} + tr\left(\widetilde{\boldsymbol{\Theta}}^T\boldsymbol{F}_\rho^{-1}\dot{\widetilde{\boldsymbol{\Theta}}}\right) \\ &= \boldsymbol{r}^T\left(-\boldsymbol{N}_0\boldsymbol{r} + \boldsymbol{M}_0\left(\ddot{\xi}_d + \boldsymbol{\Lambda}\dot{\boldsymbol{e}}\right) + \boldsymbol{N}_0\left(\dot{\xi}_d + \boldsymbol{\Lambda}\boldsymbol{e}\right) + \boldsymbol{G}_0 + \boldsymbol{\rho} - \boldsymbol{Q} + \boldsymbol{\delta}\right) \\ &\quad + \frac{1}{2}\boldsymbol{r}^T\dot{\boldsymbol{M}}_0\boldsymbol{r} + tr\left(\widetilde{\boldsymbol{\Theta}}^T\boldsymbol{F}_\rho^{-1}\dot{\widetilde{\boldsymbol{\Theta}}}\right) = \boldsymbol{r}^T\left(-\boldsymbol{N}_0\boldsymbol{r} + \boldsymbol{K}\boldsymbol{r} + \widetilde{\boldsymbol{\rho}} - \boldsymbol{\eta} + \boldsymbol{\delta}\right) \\ &\quad + \frac{1}{2}\boldsymbol{r}^T\dot{\boldsymbol{M}}_0\boldsymbol{r} + tr\left(\widetilde{\boldsymbol{\Theta}}^T\boldsymbol{F}_\rho^{-1}\dot{\widetilde{\boldsymbol{\Theta}}}\right) = \boldsymbol{r}^T\left(-\boldsymbol{K}\boldsymbol{r} + \widetilde{\boldsymbol{\rho}} - \boldsymbol{\eta} + \boldsymbol{\delta}\right) \\ &\quad + \frac{1}{2}\boldsymbol{r}^T\left(\dot{\boldsymbol{M}}_0 - 2\boldsymbol{N}_0\right)\boldsymbol{r} + tr\left(\widetilde{\boldsymbol{\Theta}}^T\boldsymbol{F}_\rho^{-1}\dot{\widetilde{\boldsymbol{\Theta}}}.\right) \end{aligned}$$

where $\left(\dot{\boldsymbol{M}}_0 - 2\boldsymbol{N}_0\right)$ is a skew-symmetric matrix, which satisfies the following equation:

$$\frac{1}{2}\boldsymbol{r}^T\left(\dot{\boldsymbol{M}}_0 - 2\boldsymbol{N}_0\right)\boldsymbol{r} = 0 \tag{9.49}$$

Because $\widetilde{\boldsymbol{\Theta}} = \boldsymbol{\Theta} - \hat{\boldsymbol{\Theta}}$, we have $\dot{\widetilde{\boldsymbol{\Theta}}} = \circ\dot{\boldsymbol{\Theta}}$.. Substituting it with Eq. (9.49) into $\dot{V}$, we have:

$$\dot{V} = -\boldsymbol{r}^T\boldsymbol{K}\boldsymbol{r} + \boldsymbol{r}^T(\widetilde{\boldsymbol{\rho}} - \boldsymbol{\eta} + \boldsymbol{\delta}) + tr\left(\widetilde{\boldsymbol{\Theta}}^T\boldsymbol{F}_\rho^{-1}\dot{\widetilde{\boldsymbol{\Theta}}}.\right) \tag{9.50}$$

Considering the adaptive law Eqs. (9.41) and (9.50) can be derived as:

$$\begin{aligned}
\dot{V} &= -\boldsymbol{r}^T\boldsymbol{K}\boldsymbol{r} + \boldsymbol{r}^T(\widetilde{\boldsymbol{\rho}} - \boldsymbol{\eta} + \boldsymbol{\delta}) - tr\left(\widetilde{\boldsymbol{\Theta}}^T\boldsymbol{F}_\rho^{-1}\left(\boldsymbol{F}_\rho\boldsymbol{\Phi}_\rho\boldsymbol{r}^T - k_\rho\boldsymbol{F}_\rho\|\boldsymbol{r}\|\circ\boldsymbol{\Theta}\right)\right) \\
&= -\boldsymbol{r}^T\boldsymbol{K}\boldsymbol{r} + \boldsymbol{r}^T(\widetilde{\boldsymbol{\rho}} - \boldsymbol{\eta} + \boldsymbol{\delta}) - tr\left(\widetilde{\boldsymbol{\Theta}}^T\left(\boldsymbol{\Phi}_\rho\boldsymbol{r}^T - k_\rho\|\boldsymbol{r}\|\circ\boldsymbol{\Theta}\right)\right) \\
&= -\boldsymbol{r}^T\boldsymbol{K}\boldsymbol{r} + \boldsymbol{r}^T(\widetilde{\boldsymbol{\rho}} - \boldsymbol{\eta} + \boldsymbol{\delta}) - tr\left(\widetilde{\boldsymbol{\Theta}}^T\boldsymbol{\Phi}_\rho\boldsymbol{r}^T\right) - tr\left(\widetilde{\boldsymbol{\Theta}}^T\left(-k_\rho\|\boldsymbol{r}\|\circ\boldsymbol{\Theta}\right)\right) \\
&= -\boldsymbol{r}^T\boldsymbol{K}\boldsymbol{r} + \boldsymbol{r}^T(\widetilde{\boldsymbol{\rho}} - \boldsymbol{\eta} + \boldsymbol{\delta}) - \boldsymbol{r}^T\left(\widetilde{\boldsymbol{\Theta}}^T\boldsymbol{\Phi}_\rho\right) + tr\left(\widetilde{\boldsymbol{\Theta}}^T\left(k_\rho\|\boldsymbol{r}\|\circ\boldsymbol{\Theta}\right)\right) \\
&= -\boldsymbol{r}^T\boldsymbol{K}\boldsymbol{r} + \boldsymbol{r}^T(-\boldsymbol{\eta} + \boldsymbol{\delta}) + k_\rho\|\boldsymbol{r}\|\cdot tr\left(\widetilde{\boldsymbol{\Theta}}^T\left(\boldsymbol{\Theta} - \widetilde{\boldsymbol{\Theta}}\right)\right)
\end{aligned} \tag{9.51}$$

where $tr\left(\widetilde{\boldsymbol{\Theta}}^T\left(\boldsymbol{\Theta} - \widetilde{\boldsymbol{\Theta}}\right)\right)$ satisfies the following inequality:

$$\begin{aligned}
tr\left(\widetilde{\boldsymbol{\Theta}}^T\left(\boldsymbol{\Theta} - \widetilde{\boldsymbol{\Theta}}\right)\right) &= \left(\widetilde{\boldsymbol{\Theta}}, \boldsymbol{\Theta}\right)_F - \|\widetilde{\boldsymbol{\Theta}}\|_F^2 \\
&\le \|\widetilde{\boldsymbol{\Theta}}\|_F\cdot\|\widetilde{\boldsymbol{\Theta}}\|_F - \|\widetilde{\boldsymbol{\Theta}}\|_F^2 \\
&\le \|\widetilde{\boldsymbol{\Theta}}\|_F\left(\boldsymbol{\Theta}_{\max} - \|\widetilde{\boldsymbol{\Theta}}\|_F\right)
\end{aligned} \tag{9.52}$$

Besides, the robust term in Eq. (9.42) satisfies the following inequality:

$$\boldsymbol{r}^T(-\boldsymbol{\eta} + \boldsymbol{\delta}) = \boldsymbol{r}^T(-\eta_{\boldsymbol{\delta}}\cdot\mathrm{sgn}(\boldsymbol{r}) + \boldsymbol{\delta}) \le 0 \tag{9.53}$$

Substituting it with Eq. (9.52) into (9.51), we have:

$$\dot{V} \le -\boldsymbol{K}_{\max}\|\boldsymbol{r}\|^2 + k_\rho\|\boldsymbol{r}\|\cdot\|\widetilde{\boldsymbol{\Theta}}\|_F\left(\boldsymbol{\Theta}_{\max} - \|\widetilde{\boldsymbol{\Theta}}\|_F\right) \tag{9.54}$$

To guarantee $\dot{V} \le 0$, $\boldsymbol{K}_{\max}\|\boldsymbol{r}\| \ge k_\rho\cdot\|\widetilde{\boldsymbol{\Theta}}\|_F\left(\boldsymbol{\Theta}_{\max} - \|\widetilde{\boldsymbol{\Theta}}\|_F\right)$ must be satisfied. The following inequality holds:

$$\|\widetilde{\boldsymbol{\Theta}}\|_F\left(\boldsymbol{\Theta}_{\max}-\|\widetilde{\boldsymbol{\Theta}}\|_F\right)=-\left(\|\widetilde{\boldsymbol{\Theta}}\|_F-\frac{\boldsymbol{\Theta}_{\max}}{2}\right)^2+\frac{\boldsymbol{\Theta}_{\max}^2}{4}\leq\frac{\boldsymbol{\Theta}_{\max}^2}{4} \tag{9.55}$$

It can be seen that when $\boldsymbol{K}_{\max}\|\boldsymbol{r}\|\geq k_\rho\frac{\boldsymbol{\Theta}_{\max}^2}{4}$, $\dot{V}\leq 0$ holds and the closed-system stability is uniformly ultimately bounded according to the Lassalle-Yoshizawa Theorem.

9.3 NUMERICAL SIMULATION

Assume orbital angular velocity ω of the space platform is 0.001033 rad/s. The -V-bar capture is adopted and the initial position of the target is (0,200) m with an initial linear velocity of (0, 0.01) m/s. The target has an initial attitude of 0 degree and rotates at an angular velocity of 1.15 degrees/s. Besides, the mass of the target is assumed to be 500 kg and has an inertial matrix of 40 kg m^2 (I_z). Two points, t_1 and t_2, of the capture component on the target are located at (0.08,−1) m with a radius of 0.05 m.

The nominal mass of the TSR is 25 kg and the actual mass 20 kg. Correspondingly, the nominal and actual inertial matrices are 0.36 and 0.3 kg m^2, respectively. Assume the nominal position of the tether attachment point in the TSR body frame is (0,0.3) m and the actual value (0,0.25) m. The parameters of the gripper are as follows: $l_1=l_2=l_5=0.25$ m, $l_2=l_4=l_6=0.20$ m. Impact parameter k_g is set to be 500 N/m and k_c zero.

The initial values of the space tether are: $l=198.25$ m, $\alpha=90$ degrees, $\dot{l}=0$ m/s, $\dot{\alpha}=0$ degrees/s; The initial attitude of the TSR are: $\psi=90$ degrees, $\dot{\psi}=5$ degrees/s. Besides, the initial joint angles $\gamma_1=\gamma_3=120$ degrees, $\gamma_2=\gamma_4=120$ degrees; During target capture phase, γ_1 and γ_3 all decrease at a speed of −2 degrees/s, and γ_2 and γ_4 keep constant.

In this study, two controllers are simulated and the results are compared. Three controllers are:

(1) Adaptive and robust target capture controller Eq. (9.37) (ARTC).

(2) Target capture controller without adaptation of TSR uncertainty $\circ\boldsymbol{\rho}$ and robust compensation term $\boldsymbol{\eta}$: $\boldsymbol{Q}=\boldsymbol{K}\boldsymbol{r}+\boldsymbol{M}_0\left(\ddot{\xi}_d+\boldsymbol{\Lambda}\dot{\boldsymbol{e}}\right)+\boldsymbol{N}_0\left(\dot{\xi}_d+\boldsymbol{\Lambda}\boldsymbol{e}\right)+\boldsymbol{G}_0$(TC).

The parameters in the target capture controller are selected as shown in Table 9.1 and the detailed simulation results are provided as follows:

Table 9.1 Target capture controller parameters

Parameters	Values	Parameters	Values
M_d	diag(1,1,1)	η_δ	0.02
B_d	diag(5,5,5)	F_ρ	diag(0.01,0.01,0.01)
K_d	diag(100,100,100)	k_ρ	0.01
Λ	diag(2,0.5,1)	ε	0.001
K	diag(0.3,4.5,0.3)		

Fig. 9.6 denotes the comparison of trajectory tracking using TC and ARTC during Target capture by the TSR, respectively. It can be seen that the trajectory tracking error of TC during target capture is obviously more remarkable than that of ARTC, which shows a better performance. Detailed numerical results are shown and analyzed as follows.

Fig. 9.7 provides the simulation results of TSR attitude ψ, and Fig. 9.8 provides the corresponding tracking errors during target capture. From the comparisons in Figs. 9.7 and 9.8, one can observe that the tracking control of the attitude for the TSR can be realized by both TC and ARTC. The convergence time of TC is about 44 s, while that of ARTC is about 15 s, 29 s shorter than the former. Moreover, between these two methods, ARTC achieves better transient performance with smaller amplitudes and oscillations during the target capture.

Fig. 9.9 shows the simulation results of an in-plane angle of the space tether during target capture and Fig. 9.10 is the tracking errors of α. It can be seen that the convergence time of ARTC and TC are 33 and 40 s, respectively, for α stabilizing within ± 0.01 degrees, which suggests that the ARTC converges faster. Besides, the overshoot of TC is about -0.083 degrees, 0.014 degrees bigger than that of ARTC, which is about -0.069 degrees.

A comparison of the space tether length between ARTC and TC can be observed in Figs. 9.11 and 9.12. After 13 s, the tether length of ARTC converges within ± 0.01 m. However, TC has a longer convergence time of 33 s with a steady tracking error of 0.035 m, which is almost three times that of the former.

Fig. 9.13 provides simulation results of the velocities of attitude, in-plane angle, and length and Fig. 9.14 provides the comparison of the error function r for both ARTC and TC.

Figs. 9.15–9.19 compare the impact forces of ARTC and TC between the gripper of the TSR and target during capture operation. The simulation results suggest that the collisions mainly occur on a_0a_1, b_0b_1, c_1c_2 of the TSR's

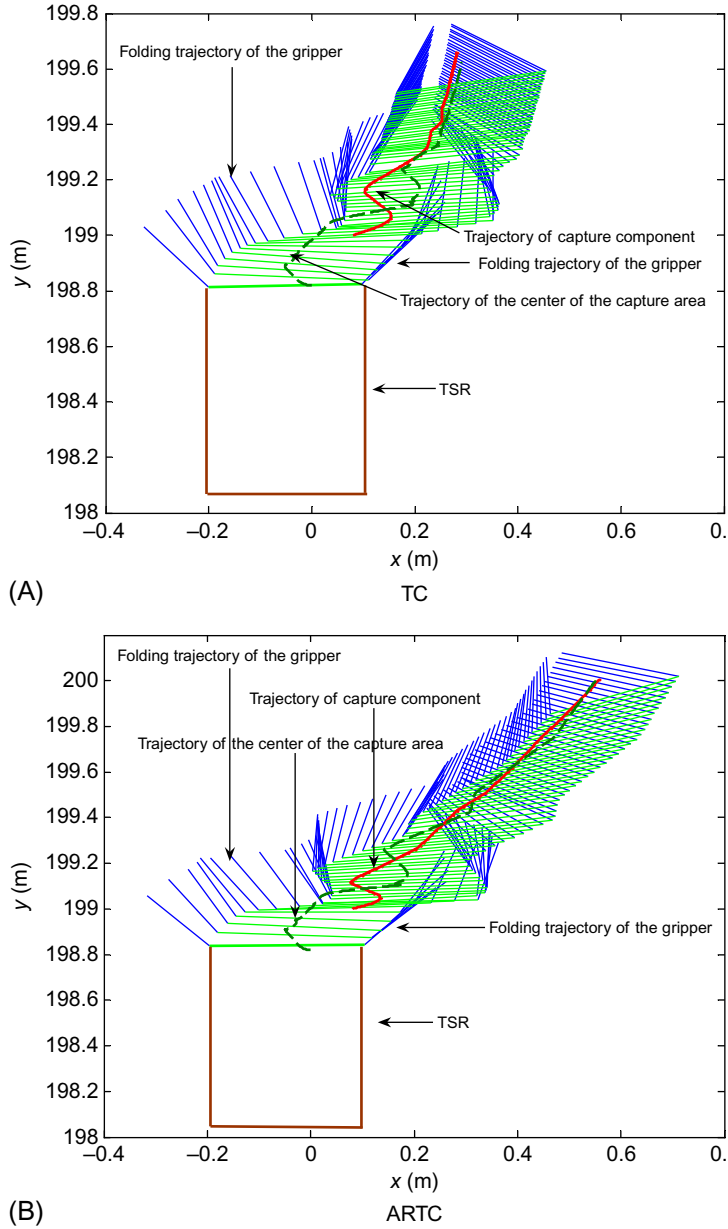

Fig. 9.6 Comparison of trajectory tracking using (A) TC and (B) ARTC during target capture.

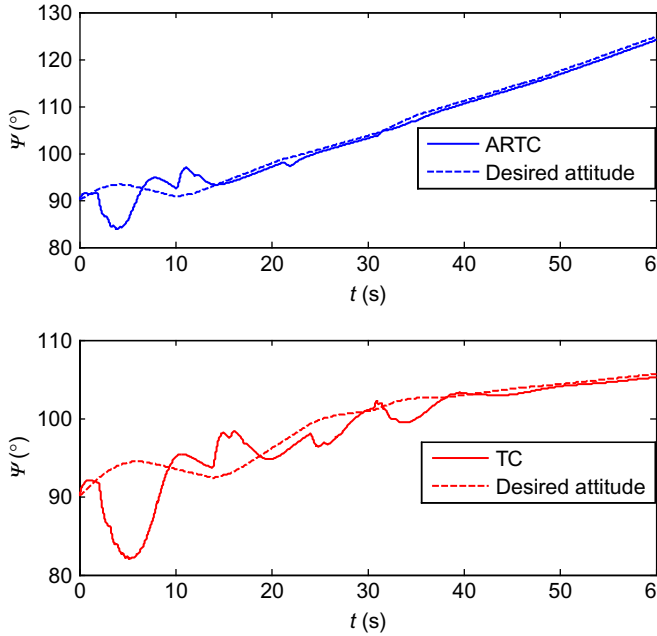

Fig. 9.7 Attitude of TSR during target capture.

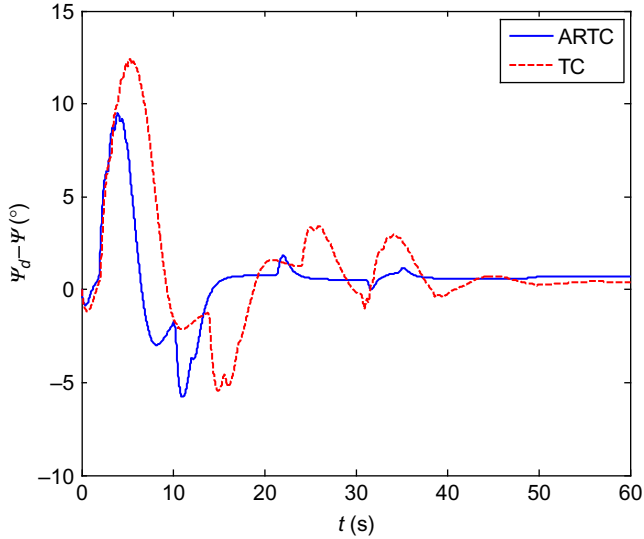

Fig. 9.8 Tracking errors of ψ during target capture.

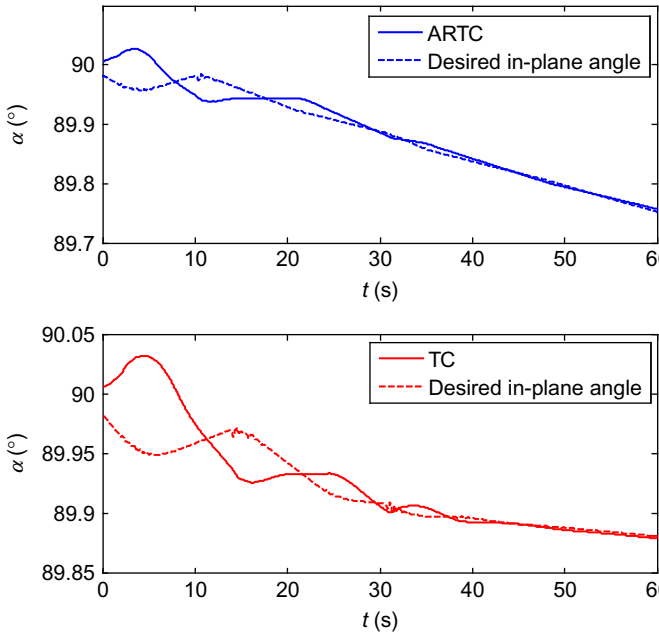

Fig. 9.9 In-plane angle of the space tether during target capture.

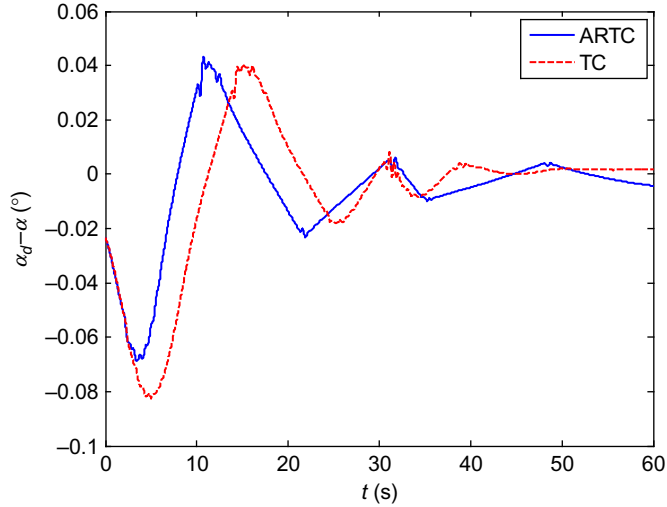

Fig. 9.10 Tracking errors of α during target capture.

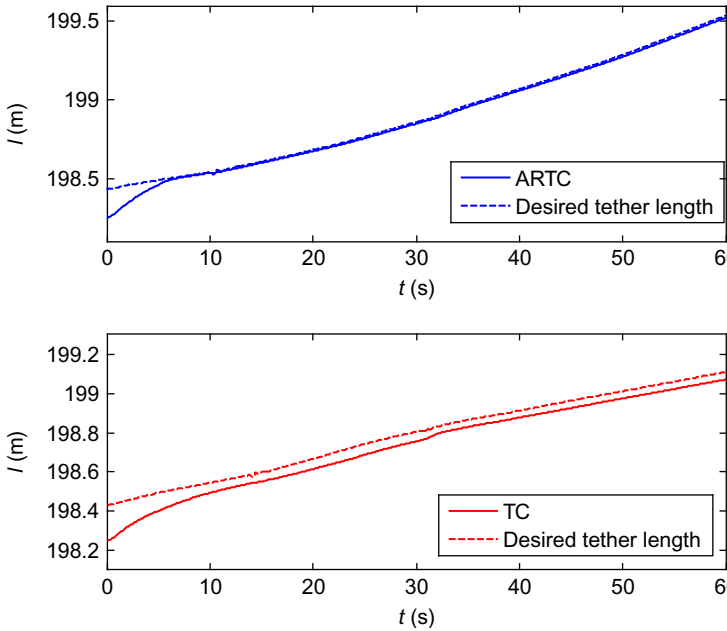

Fig. 9.11 Length of space tether during target capture.

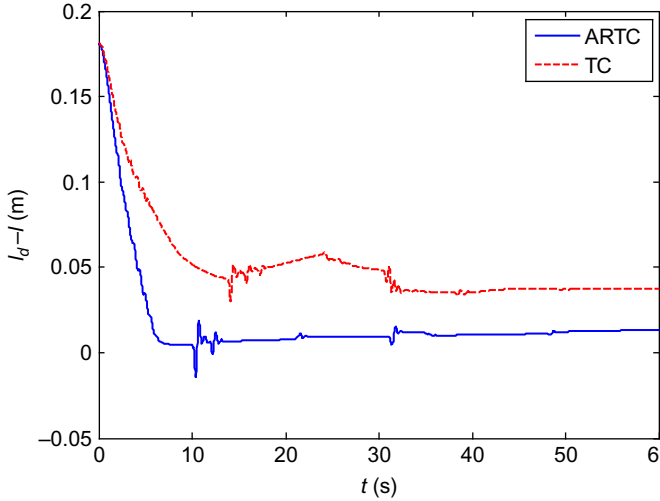

Fig. 9.12 Tracking errors of *l* during target capture.

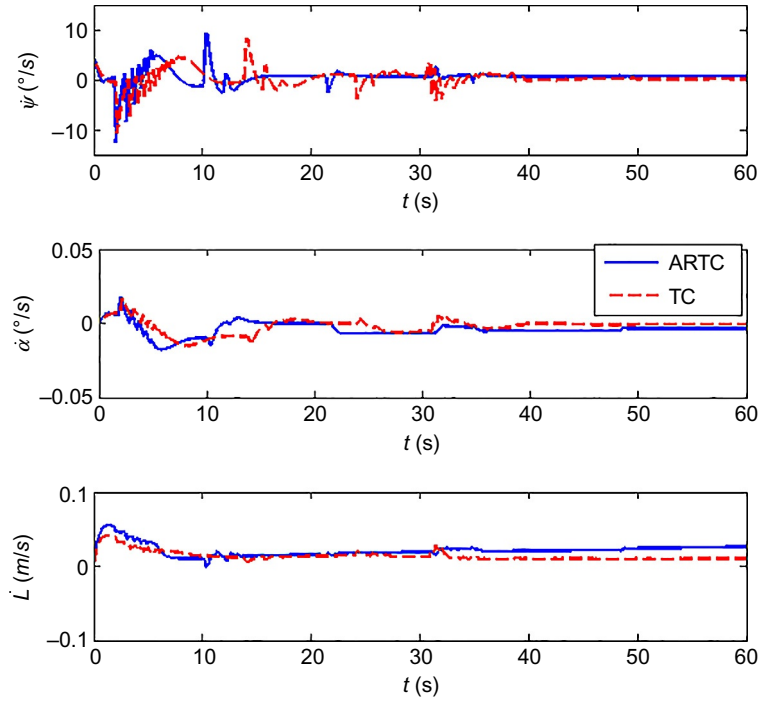

Fig. 9.13 Velocities of attitude, in-plane angle, and length.

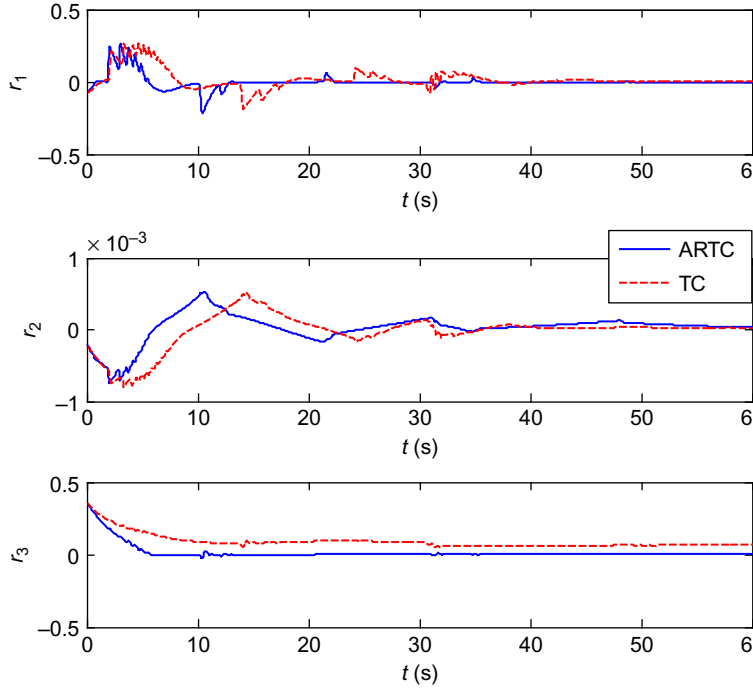

Fig. 9.14 Error function *r*.

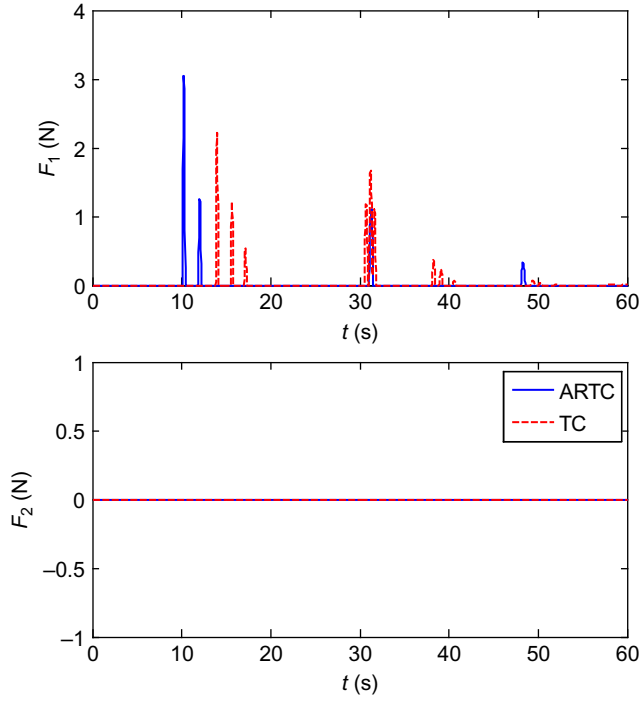

Fig. 9.15 Impact forces on $a_0a_1a_2$ of the TSR's gripper.

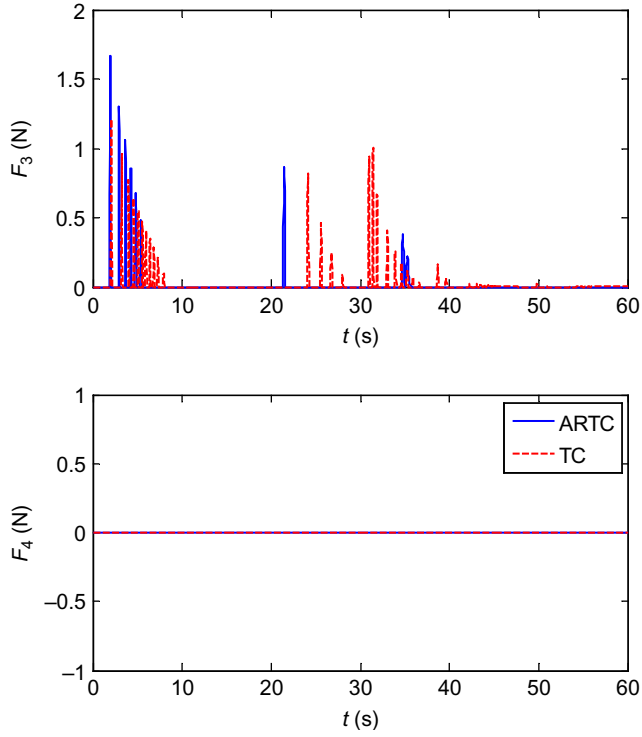

Fig. 9.16 Impact forces on $b_0b_1b_2$ of the TSR's gripper.

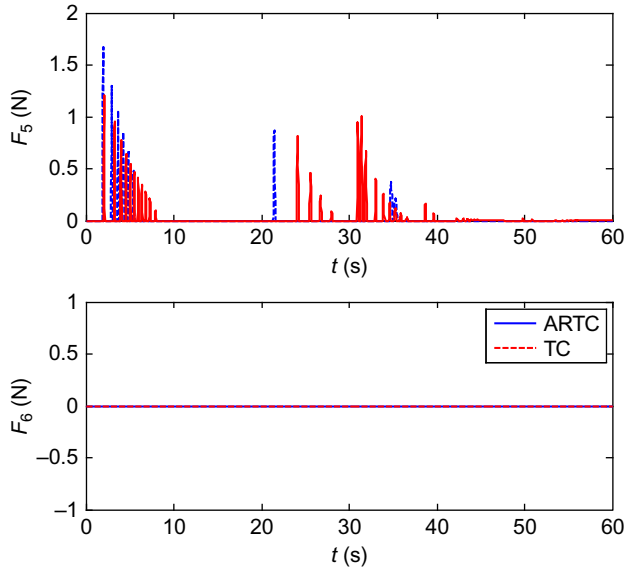

Fig. 9.17 Impact forces on $c_0c_1c_2$ of the TSR's gripper.

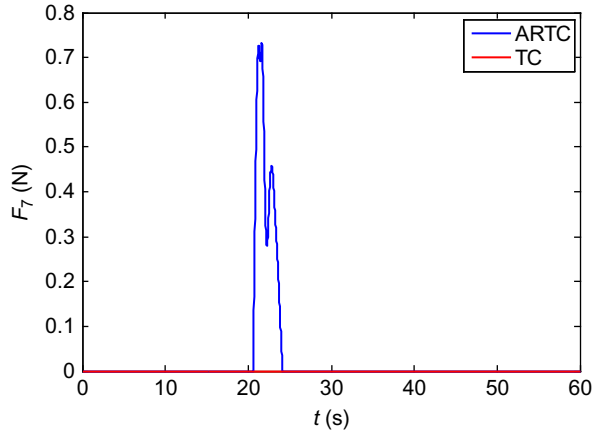

Fig. 9.18 Impact forces on front plane of the TSR's gripper.

gripper. The magnitude of the impact forces and the frequency of collisions are almost the same before 20 s. However, in 20 s, collisions of TC between the gripper of the TSR and the target are clearly more frequent than those of ARTC. The main reason for this phenomenon is that the higher overshoots and bigger tracking errors of TC lead to more collisions between the gripper

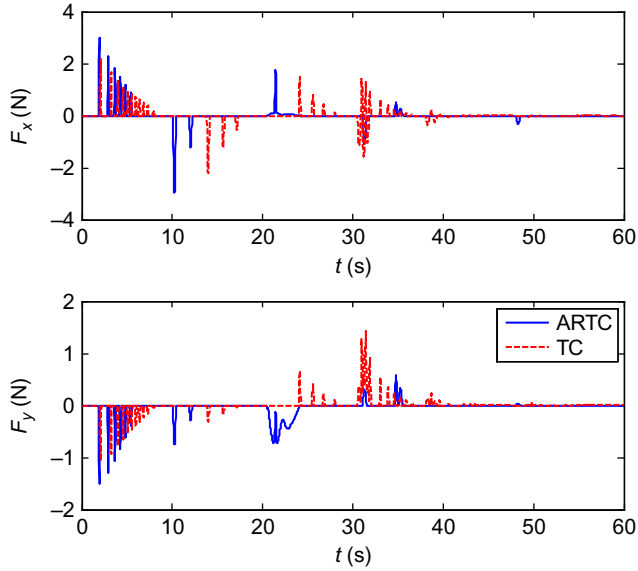

Fig. 9.19 Overall impact forces between gripper of the TSR and the target.

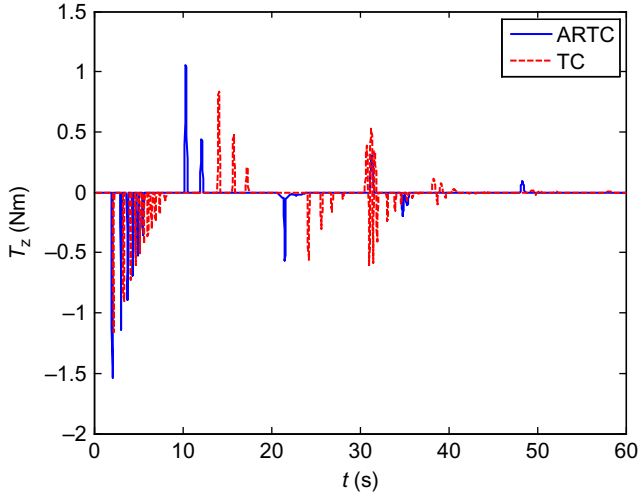

Fig. 9.20 Overall impact torques between gripper of the TSR and the target.

of the TSR and the target, which is suggested in the previous simulation results.

Fig. 9.19 shows the overall impact forces exerted on the gripper of the TSR and Fig. 9.20 the corresponding overall impact torques during target capture. The similar conclusion can be drawn that compared with ARTC,

more impact forces and torques of TC during 20–60 s are generated due to the higher overshoots and bigger tracking errors, which are not beneficial for the target capture mission. This demonstrates that ARTC is advantageous and preferable for the TSR in the target capture operation (Fig. 9.21).

Figs. 9.22 and 9.23 indicate the influence of the collision during capture on the attitude of the target, which are expressed in MRP form and Euler angle form, respectively. We can see that ψ_t of ARTC changes from initial value of 0 degrees to the final value of about 35 degrees and that of TC varies from initial value of 0 degrees to the final value of about 16 degrees. Fig. 9.24 provides the influence of the collision during capture on the position of the target. The maximum position changes of ARTC and TC are 0.77 and 0.62 m along x-axis, respectively. Although these values cannot be directly used to determine which controller is better, we can conclude that for a target that is spinning and moving, the target capture by the TSR can still be achieved by ARTC proposed in this chapter.

This chapter presents an adaptive robust controller to achieve target capture by the TSR. The numerical simulations show that the proposed

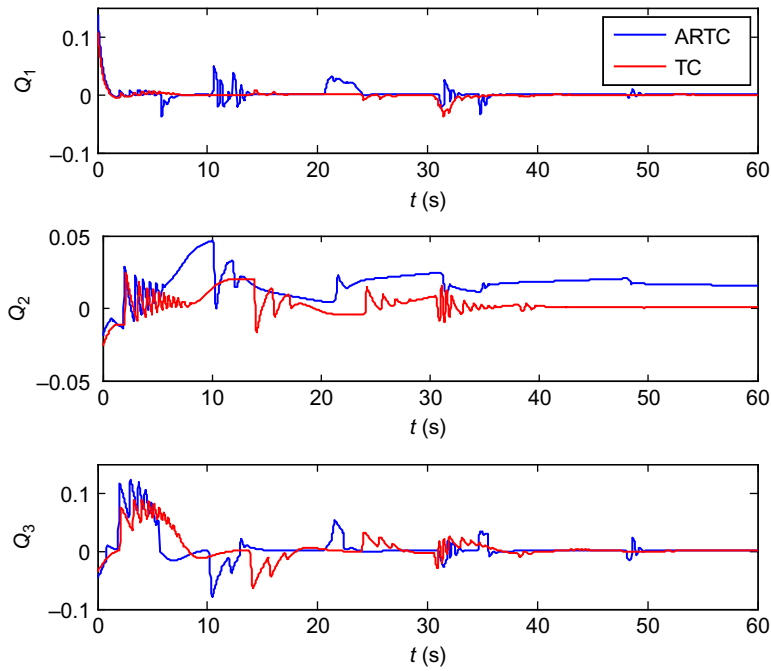

Fig. 9.21 Control input of the TSR for target capture.

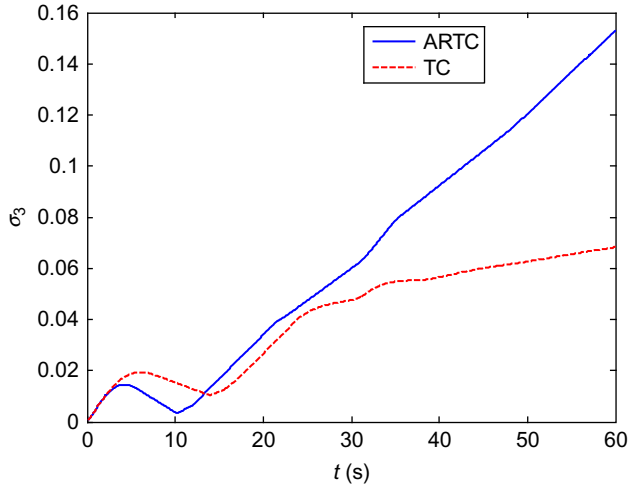

Fig. 9.22 Attitude σ_e of the target during capture.

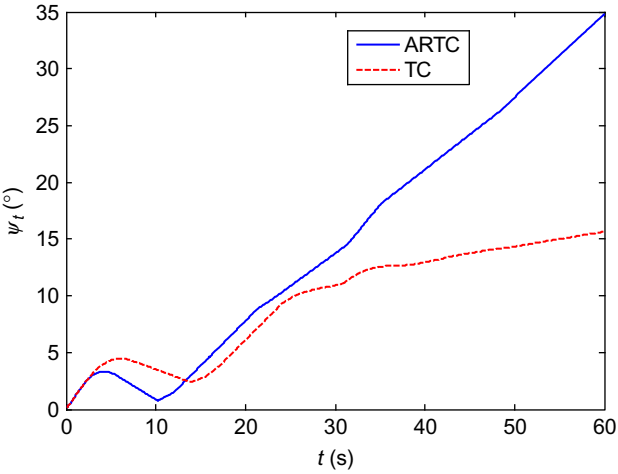

Fig. 9.23 Euler angle of the target attitude during capture.

adaptive and robust controller based on impedance control can realize the stabilization of the TSR during target capture. Compared to the target capture controller without adaptation and robust term, the NN-based adaptive law can compensate the uncertainty in the dynamic model of the TSR and realize strong control performance with a smaller overshoot, less convergence time, and higher control accuracy.

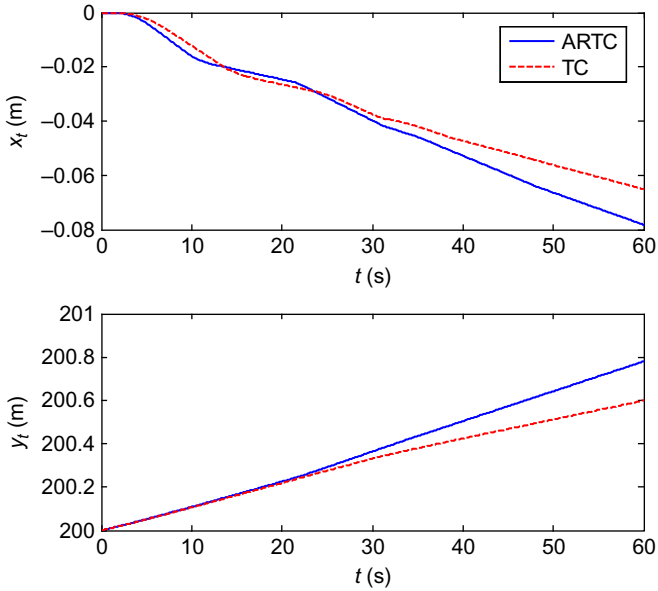

Fig. 9.24 Position change of the target during capture.

REFERENCES

[1] Y. Nakamura, F. Sasaki, S. Nakasuka, Guidance and control of tethered retriever with collaborative tension-thruster control for future on-orbit service missions, in: Proceedings of the 8th International Symposium on Artificial Intelligence, Robotics and Automation in Space (i-SAIRAS 2005), 2005.

[2] V.J. Modi, S. Pradhan, A.K. Misra, Off-set control of the tethered systems using a graph theoretic approach, Acta Astronaut. 35 (6) (1995) 373–384.

[3] K.K. Mankala, S.K. Agrawal, A boundary controller based on linear infinite dimensional system for station keeping of a tethered satellite system, in: IEEE American Control Conference 2006, 2006.

[4] M. Nohmi, T. Yamamoto, Y. Takagi, Microgravity experiment for attitude control of a tethered body by arm link motion, in: IEEE International Conference on Mechatronics and Automation 2007, ICMA 2007, 2007.

[5] M. Nohmi, Attitude control of a tethered space robot by link motion under microgravity, Proceedings of the 2004 IEEE International Conference on Control Applications, vol. 1, (2004).

[6] M. Nohmi, Mission design of a tethered robot satellite "STARS" for orbital experiment, in: 2009 IEEE Control Applications (CCA) & Intelligent Control (ISIC), 2009.

[7] S. Bergamaschi, F. Bonon, Coupling of tether lateral vibration and subsatellite attitude motion, J. Guid. Control. Dyn. 15 (5) (1992) 1284–1286.

[8] D. Wang, et al., Coordinated control of tethered space robot using mobile tether attachment point in approaching phase, Adv. Space Res. 54 (6) (2014) 1077–1091.

[9] M. Makarov, et al., Adaptive filtering for robust proprioceptive robot impact detection under model uncertainties, IEEE/ASME Trans. Mechatron. 19 (6) (2014) 1917–1928.

[10] S.B. Backus, A.M. Dollar, Robust resonant frequency-based contact detection with applications in robotic reaching and grasping, IEEE/ASME Trans. Mechatron. 19 (5) (2014) 1552–1561.
[11] L.-B. Wee, M.W. Walker, On the dynamics of contact between space robots and configuration control for impact minimization, IEEE Trans. Robot. Autom. 9 (5) (1993) 581–591.
[12] F. Aghili, Pre-and post-grasping robot motion planning to capture and stabilize a tumbling/drifting free-floater with uncertain dynamics, in: 2013 IEEE International Conference on Robotics and Automation (ICRA), IEEE, 2013.
[13] K. Yoshida, D. Dimitrov, H. Nakanishi, On the capture of tumbling satellite by a space robot, in: IEEE/RSJ International Conference on Intelligent Robots and Systems, 2006, IEEE, 2006.
[14] P. Huang, Y. Xu, B. Liang, Balance control of multi-arm free-floating space robots during capture operation, in: 2005 IEEE International Conference on Robotics and Biomimetics (ROBIO), IEEE, 2005.
[15] W. Xu, Y. Liu, Y. Xu, The coordinated motion planning of a dual-arm space robot for target capturing, Robotica 30 (05) (2012) 755–771.
[16] Z.H. Luo, Y. Sakawa, Control of a space manipulator for capturing a tumbling object, in: Proceedings of the 29th IEEE Conference on Decision and Control, 1990, IEEE, 1990.
[17] R. McCourt, C.W. De Silva, Autonomous robotic capture of a satellite using constrained predictive control, IEEE/ASME Trans. Mechatron. 11 (6) (2006) 699–708.
[18] T. Oki, H. Nakanishi, K. Yoshid, Whole-body motion control for capturing a tumbling target by a free-floating space robot, in: IEEE/RSJ International Conference on Intelligent Robots and Systems 2007 (IROS 2007), IEEE, 2007.
[19] F. Aghili, A prediction and motion-planning scheme for visually guided robotic capturing of free-floating tumbling objects with uncertain dynamics, IEEE Trans. Robot. 28 (3) (2012) 634–649.
[20] F. Aghili, Optimal control for robotic capturing and passivation of a tumbling satellite with unknown dynamics, in: AIAA Guidance, Navigation, and Control Conference and Exhibit, vol. 21, 2008.
[21] P. Huang, et al., Robust control of space robot for capturing objects using optimal control method, in: International Conference on Information Acquisition 2007, ICIA'07, IEEE, 2007.
[22] A. Flores-Abad, et al., Optimal control of space robots for capturing a tumbling object with uncertainties, J. Guid. Control. Dyn. 37 (6) (2014) 2014–2017.
[23] S.A.A. Moosavian, R. Rastegari, Multiple-arm space free-flying robots for manipulating objects with force tracking restrictions, Robot. Auton. Syst. 54 (10) (2006) 779–788.
[24] S.A. Moosavian, R. Rastegari, E. Papadopoulos, Multiple impedance control for space free-flying robots, J. Guid. Control. Dyn. 28 (5) (2005) 939–947.
[25] H. Nakanishi, K. Yoshida, Impedance control for free-flying space robots-basic equations and applications, in: IEEE/RSJ International Conference on Intelligent Robots and Systems, 2006, IEEE, 2006.
[26] S. Abiko, R. Lampariello, G. Hirzinger, Impedance control for a free-floating robot in the grasping of a tumbling target with parameter uncertainty, in: IEEE/RSJ International Conference on Intelligent Robots and Systems, 2006, IEEE, 2006.
[27] W. Cheng, L. Tianxi, Z. Yang, Grasping strategy in space robot capturing floating target, Chin. J. Aeronaut. 23 (5) (2010) 591–598.
[28] J.-J.E. Slotine, W. Li, On the adaptive control of robot manipulators, Int. J. Robot. Res. 6 (3) (1987) 49–59.
[29] T. Valency, M. Zacksenhouse, Accuracy/robustness dilemma in impedance control, J. Dyn. Syst. Meas. Control. 125 (3) (2003) 310–319.
[30] F.L. Lewis, K. Liu, A. Yesildirek, Neural net robot controller with guaranteed tracking performance, IEEE Trans. Neural Netw. 6 (3) (1995) 703–715.